

Coarse-Grained Geometric Quantum Dynamics in the Tensor Network Representation

Mo Sha¹ and Bing Gu^{1,*}

¹*Department of Chemistry and Department of Physics,
Westlake University, Hangzhou, Zhejiang, China, 310030*

Quantum geometrical molecular dynamics provides a quantum geometric picture for understanding reactive dynamics, especially excited-state conical intersection dynamics, and also a numerically exact method for strongly correlated electron-nuclear dynamics. However, there are substantial challenges in describing medium-size molecules with tens of nuclear degrees of freedom. The main challenge is that it uses a discrete variable representation to discretize the molecular configuration space, and thus requires a tremendous number of quantum chemistry calculations to construct the electronic overlap matrix. Moreover, the expansion coefficients scale exponentially with molecular size for direct-product basis sets. We address these challenges by first introducing a coarse-grained local diabatic ansatz, followed by a tensor network representation of the expansion coefficients and the molecular time-evolution operator. With a full 24-dimensional demonstration using the pyrazine molecule, we show that such developments provide a highly accurate and computationally tractable method for high-dimensional, fully quantum, strongly coupled electron-nuclear dynamics from first principles.

The conventional understanding of chemistry is based on the Born–Oppenheimer approximation for ground-state calculation and the Born–Huang framework for nonadiabatic excited-state processes, exploiting the timescale separation between electrons and nuclei. In the Born–Oppenheimer dynamics, the nuclear motion is entirely determined by the landscape of the adiabatic potential energy surface (APES). non–Born–Oppenheimer effects, including nonradiative electronic transitions, the geometric phase effect, and diagonal Born–Oppenheimer corrections essential for excited-state conical intersection dynamics, are accounted for by first- and second-order derivative couplings and vector potentials [1]. However, all such corrections, despite being of order $\mathcal{O}(M^{-1})$, diverge at electronic degeneracies, particularly at conical intersections.

Conical intersections are hypersurfaces on the APESs of polyatomic molecules where two or more electronic states become degenerate. They can act as efficient “molecular funnels” mediating ultrafast non-radiative transitions on the femtosecond (10^{-15} s) timescale and play a fundamental role in photophysics, photochemistry, and photobiology, such as in the primary event of vision, the photostability of DNA molecules, and energy conversion in photosynthesis [2–8]. Moreover, the geometric phase effects can lead to destructive interference in the nuclear motion that can significantly influence the outcome of reactive scattering, cold chemistry, and photodissociation [9–14]. To model and predict these ultrafast conical intersection dynamics, it is essential to go beyond the Born–Oppenheimer approximation and takes fully account of the strong electron-nuclear correlation in the course of dynamics.

The singular derivative couplings make the Born–Huang framework inappropriate for CI dynamics. One

approach for treating conical intersection dynamics is through an adiabatic-to-diabatic transformation. Strict diabatization is impossible for a finite number of electronic states due to geometric obstruction [15]. Instead, many quasi-diabatization schemes depending on different criteria, which cannot be uniquely defined and are often not straightforward to use, have to be employed to construct a diabatic model, followed by accurate quantum wavepacket propagation on this diabatic potential energy surface [16–22]. However, these methods face a series of severe challenges in practical applications. One of the most fundamental obstacles is the “curse of dimensionality”: the computational resources (memory and computation time) required to accurately describe a molecular wavefunction grow exponentially with the number of degrees of freedom. This makes full-dimensional, numerically exact simulations infeasible for all but the smallest molecules (typically with fewer than six degrees of freedom). A simpler approach is to construct a vibronic coupling model Hamiltonian, usually based on the crude adiabatic representation. The advantage is that it is possible to treat such analytical models with tens of nuclear degrees of freedom using a tensor network representation of the nuclear wavefunction, as in the multi-configuration time-dependent Hartree and time-dependent density-matrix renormalization group [23–27]. While such methods are powerful for high-dimensional quantum dynamics, their application requires pre-constructed, global diabatic model Hamiltonians. Thus, this approach mainly focuses on photophysical processes involving only small-amplitude motion, such as in molecular aggregates and crystals [28–30].

Quantum geometrical molecular dynamics is a quantum geometric framework for both ground-state and excited-state chemistry that emphasizes a global view of the molecular fiber bundle [31]. It retains the chemically highly intuitive and useful concept of APES but differs fundamentally from the Born–Huang framework in how the non–Born–Oppenheimer effects are described.

* gubing@westlake.edu.cn

In this geometric framework, *all* non-Born–Oppenheimer effects are unified into a single term—the global overlap matrix of adiabatic electronic states. Unlike the Born–Huang representation, which suffers from singular derivative couplings, the overlap matrix remains bounded throughout the entire configuration space, even in systems with conical intersections. Therefore, the quantum geometrical molecular dynamics provides a numerically exact and singularity-free method for modeling non-adiabatic conical intersection dynamics. The geometric approach is based on the local diabatic ansatz, with the nuclear motion described by a discrete variable representation (DVR) and the electronic motion by adiabatic states at the DVR grid points[32–34]. Note that the local diabatic ansatz is not a quasi-diabatization scheme but directly uses the electronic eigenstates. One of the main practical advantages is that it does not even require a smooth gauge fixing of the electronic states [35], making it straightforward for *ab initio* simulations because the output of any quantum chemistry method inevitably carries random signs (or phases) depending on the gauge group[1, 36]. Despite its conceptual and practical advantages for strongly correlated electron-nuclear dynamics, the computational cost scales exponentially with the number of nuclear degrees of freedom. Prior work has sought to mitigate this issue by employing Smolyak sparse-grid discretization to reduce the number of grid points and linked product approximation to reduce costly electronic-structure calculations [37, 38]. However, the geometric approach is still computationally infeasible for medium-size molecules with dozens of degrees of freedom.

Here we introduce a coarse-grained local diabatic ansatz that is suitable for high-dimensional nonadiabatic quantum molecular dynamics with only adiabatic electronic input. Furthermore, within the coarse-grained ansatz, we employ a tensor network representation—specifically, the matrix product state for the expansion coefficients and the matrix product operator for the total molecular time-evolution operator. We first benchmark its accuracy and efficiency against numerically exact quantum geometrical molecular dynamics calculations on a reduced four-mode model of internal conversion in pyrazine. The power of our approach is then demonstrated by applying it to the full 24-mode pyrazine model, showcasing its ability to tackle complex, high-dimensional conical intersection problems.

Quantum Geometrical Molecular Dynamics— In the quantum geometrical molecular dynamics, the equation of motion is given by [31],

$$i\frac{\partial\chi(\mathbf{R},t)}{\partial t} = \int d\mathbf{R}' T(\mathbf{R}, \mathbf{R}') \mathbf{A}(\mathbf{R}, \mathbf{R}') \chi(\mathbf{R}', t) + \mathbf{V}(\mathbf{R}) \chi(\mathbf{R}, t) \quad (1)$$

where $T(\mathbf{R}, \mathbf{R}') = \langle \mathbf{R} | \hat{T}_N | \mathbf{R}' \rangle$ is the coordinate representation of the kinetic energy operator. The global electronic overlap matrix encodes the quantum geometry of

the molecular fiber bundle. Specifically, it is the generating function of all non-Abelian quantum geometric measures. The first order contains the Berry connection and first-order derivative couplings, and the second order contains the non-Abelian quantum geometric tensor. It can be generated to non-Hermitian Hamiltonians [31].

The integro-differential equation can be discretized by the local diabatic ansatz,

$$\Psi(\mathbf{r}, \mathbf{R}, t) = \sum_{\mathbf{n}, \alpha} C_{\mathbf{n}\alpha}(t) \phi_{\alpha}(\mathbf{r}; \mathbf{R}_n) \chi_{\mathbf{n}}(\mathbf{R}), \quad (2)$$

where $\chi_{\mathbf{n}}(\mathbf{R}) = \chi_{n_1}(R_1) \cdots \chi_{n_d}(R_d)$ with $\mathbf{n} = (n_1, \dots, n_d)$ is the discrete variable representation (DVR) basis set defining a set of grid points (i.e., configurations) $\{\mathbf{R}_n\}$ [32, 33], $\phi_{\alpha}(\mathbf{r}; \mathbf{R}_n)$ denotes the associated electronic eigenstates (i.e., eigenstates of the electronic Hamiltonian at \mathbf{R}_n with energies $V_{n\alpha}$), and $C_{\mathbf{n}\alpha}(t)$ are the expansion coefficients. The vibronic basis set is a direct product of a nuclear basis function $|\chi_{\mathbf{n}}\rangle$ and adiabatic electronic states $|\phi_{\alpha}(\mathbf{R}_n)\rangle$ at a fixed geometry, thus providing a discrete local trivialization of the molecular fiber bundle consisting of the truncated electronic Hilbert space parameterized by the configuration space. We use a shorthand notation $|\mathbf{n}\alpha\rangle \equiv |\phi_{\alpha}(\mathbf{R}_n)\rangle \otimes |\chi_{\mathbf{n}}\rangle$. The local diabatic ansatz leverages the locality and orthonormality of the DVR basis to simplify the construction of electronic Hamiltonian matrix elements. This is particularly important for *ab initio* modeling with the molecular Coulomb Hamiltonian, where the construction is significantly more challenging than for a model Hamiltonian. The electronic Hamiltonian are diagonal in the DVR set $\langle \mathbf{m}\beta | \hat{H}_{\text{BO}}(\mathbf{r}; \mathbf{R}) | \mathbf{n}\alpha \rangle = V_{n\alpha} \delta_{mn} \delta_{\beta\alpha}$. A unique feature of the geometric approach is that the nuclear kinetic energy operator, \hat{T}_N , acting solely on the nuclear space, is dressed by the electronic overlap matrix

$$\langle \mathbf{m}\beta | \hat{T}_N | \mathbf{n}\alpha \rangle = A_{\mathbf{m}\beta, \mathbf{n}\alpha} T_{mn} \quad (3)$$

Here, $T_{mn} = \langle \mathbf{m} | \hat{T}_N | \mathbf{n} \rangle$ is the kinetic energy matrix element in the nuclear DVR basis, which often has an analytical form, and $A_{\mathbf{m}\beta, \mathbf{n}\alpha} = \langle \phi_{\beta}(\mathbf{R}_m) | \phi_{\alpha}(\mathbf{R}_n) \rangle$ is the electronic overlap matrix. Inserting the ansatz Eq. (2) into the time-dependent Schrödinger equation, $i\partial_t |\Psi(t)\rangle = \hat{H} |\Psi(t)\rangle$, and left multiplying $\langle \mathbf{m}\beta |$ yields the equation of motion

$$i\dot{C}_{\mathbf{m}\beta}(t) = V_{\beta}(\mathbf{R}_m) C_{\mathbf{m}\beta}(t) + \sum_{\mathbf{n}, \alpha} A_{\mathbf{m}\beta, \mathbf{n}\alpha} T_{mn} C_{\mathbf{n}\alpha}(t). \quad (4)$$

With a direct-product nuclear basis set, there is an apparent challenge that the expansion coefficients, $C_{\mathbf{n}\alpha}(t)$, a $(d+1)$ dimensional tensor with shape $N_0 \times N_1 \times \cdots \times N_d$, where d is the number of nuclear degrees of freedom, N_0 is the number of electronic states, and N_k is the number of basis functions for the k -th coordinate, scale exponentially with the molecular size. For this, we will employ an efficient tensor network representation. However, the most severe challenge of geometric quantum dynamics

comes from the electronic overlap matrix. Even when the expansion coefficient can be expressed by a Hartree product, it does not reduce the cost associated with the electronic overlap matrix because the molecular configuration space remains exponentially large. It is simply not possible to compute the electronic eigenstates for each configuration and construct the overlap matrix. A naive idea is to reduce the number of grid points. However, a dense grid is required to describe the nuclear dynamics because, upon photoexcitation, the electronic energy quickly flows into the nuclear degrees of freedom and the nuclear wave packet spreads quickly in the configuration space even when it is initially localized.

Coarse-Graining of the Electronic Space — We realize that the nuclear grid plays dual roles in geometric quantum dynamics. On one hand, it is used to represent the time-dependent nuclear wave packet. This usually requires a dense grid, as the nuclear kinetic energy can be large in the course of excited-state dynamics. On the other hand, the nuclear grid provides a local trivialization to describe the electronic quantum geometry. The fineness required for this purpose is determined by how the electronic states vary with nuclear geometry[31, 39]. The dynamical and geometrical grids are enforced to be equivalent in the local diabatic ansatz. The insight is that it is not necessary to use a very dense grid to describe the electronic quantum geometry, meaning there is substantial redundancy in the original ansatz. While the molecular configuration space is necessarily exponentially large, the size of the effective electronic Hilbert space is most likely not exponentially large.

For many chemical reactions (e.g., photodissociation or photoisomerization), only a few reaction coordinates undergo large amplitude motion involving bond breaking and formation, whereas the rest undergo small amplitude motion. It is expected that the electronic states do not vary significantly along those modes. It is therefore convenient to partition the full set of nuclear coordinates $\mathbf{R} = \{\mathbf{q}, \mathbf{Q}\}$ into a few primary reactive coordinates, \mathbf{q} , that undergo large amplitude motion, and the remaining non-reactive coordinates, \mathbf{Q} , with small amplitude motion. We introduce a coarse-grained local diabatic ansatz

$$|\Psi(t)\rangle = \sum_{\alpha, \mathbf{n}, \nu} C_{\alpha \mathbf{n} \nu}(t) |\phi_\alpha(\mathbf{q}_n, \mathbf{Q}_0)\rangle \otimes |\chi_n\rangle \otimes |\xi_\nu\rangle, \quad (5)$$

where $|\xi_\nu\rangle$, $\nu = (\nu_1, \nu_2, \dots, \nu_{d_{\text{NR}}})$ refers to the basis functions for the non-reactive coordinates. This ansatz differs from the original ansatz in that only a small subset of electronic states corresponding to the nuclear configurations $(\mathbf{q}_n, \mathbf{Q}_0)$ are employed rather than the complete electronic manifold corresponding to $(\mathbf{q}_n, \mathbf{Q}_\nu)$. This significantly reduces the electronic structure calculations given that the number of non-reactive modes is much larger than the number of reactive coordinates, $d_{\text{NR}} \gg d_R$. In the coarse-grained vibronic basis set, the nuclear kinetic energy matrix elements remain intact as the nuclear basis functions are not changed. However, the matrix elements of the electronic Hamiltonian

$\langle \beta \mathbf{m} \nu | \hat{H}_{\text{BO}}(\mathbf{r}; \mathbf{q}, \mathbf{Q}) | \alpha \mathbf{n} \nu \rangle$ are not diagonal anymore as a consequence of the coarse-graining. To compute its matrix elements, for the small-amplitude modes, we expand the electronic Hamiltonian at a reference point \mathbf{Q}_0 (up to the second order in this work):

$$\begin{aligned} \hat{H}_{\text{BO}}(\mathbf{r}; \mathbf{q}, \mathbf{Q}) &= \hat{H}_0(\mathbf{r}; \mathbf{q}) + \hat{\mathbf{F}}(\mathbf{r}; \mathbf{q}) \cdot \Delta \hat{\mathbf{Q}} \\ &+ \frac{1}{2} \Delta \hat{\mathbf{Q}}^\top \hat{\mathbf{G}}(\mathbf{r}; \mathbf{q}) \Delta \hat{\mathbf{Q}} \equiv \hat{H}_0 + \hat{H}_1, \end{aligned} \quad (6)$$

where $\hat{H}_0 \equiv \hat{H}_0(\mathbf{r}; \mathbf{q}) = \hat{H}_{\text{BO}}(\mathbf{r}; \mathbf{q}, \mathbf{Q}_0)$, $\hat{F}_k(\mathbf{r}; \mathbf{q}) = \partial_k \hat{H}_{\text{BO}}(\mathbf{r}; \mathbf{q}, \mathbf{Q})|_{\mathbf{Q}_0}$, $\partial_k \equiv \partial/\partial Q_k$, and $\hat{G}_{kl}(\mathbf{r}; \mathbf{q}) = \partial_k \partial_l \hat{H}_{\text{BO}}(\mathbf{r}; \mathbf{q}, \mathbf{Q})|_{\mathbf{Q}_0}$ are operators acting on the composite electronic and reactive coordinate space, and $\Delta \hat{\mathbf{Q}} = \hat{\mathbf{Q}} - \mathbf{Q}_0$. The total molecular Hamiltonian is thus partitioned as $\hat{H} = \hat{T}_N + \hat{H}_0 + \hat{H}_1$.

Matrix Product States and Operators — To circumvent the exponential growth of expansion coefficients, we represent the high-dimensional tensor $C_{\alpha \mathbf{n}}(t)$ in the tensor-train (TT) format, which is equivalently referred to as a matrix product state (MPS) in many-body physics [26, 27]:

$$C_{\alpha \mathbf{n}}(t) = \sum_{a_0, \dots, a_{d-1}} M_{a_0}^{[0]\alpha}(t) M_{a_0, a_1}^{[1]n_0}(t) \cdots M_{a_{d-1}}^{[d]n_{d-1}}(t). \quad (7)$$

Here, the first tensor $M^{[0]}$ is associated with the electronic state index α , while the subsequent tensors $M^{[k]}$ ($k = 1, \dots, d$) carry the physical indices n_{k-1} corresponding to the nuclear degrees of freedom. The virtual indices a_k (with bond dimension D_k) connect adjacent sites, encoding the entanglement structure. The MPS form can be constructed from the full tensor with controlled accuracy using the TT-SVD algorithm [40], as detailed in Algorithm S1. In this representation, we explicitly fix the inherent gauge degree of freedom to the right-canonical form. This step is essential to avoid amplified perturbation errors and reduced accuracy associated with non-canonical forms [26, 41]. Beyond gauge fixing, the ordering of sites is crucial for efficiency; strongly coupled degrees of freedom should be placed in proximity [42–44]. Guided by this principle, we order the sites as follows: the electronic states first, followed by the reactive coordinates \mathbf{q} , and finally the non-reactive coordinates \mathbf{Q} .

To propagate the wavefunction, we extend the tensor-train framework to operators by representing the $(2d + 2)$ -dimensional time-evolution operator $\hat{U}(\Delta t) = e^{-i\hat{H}\Delta t}$ as a Matrix Product Operator (MPO). As the operator-space counterpart to the MPS, the MPO expresses the propagator as a contracted chain of local tensors:

$$U_{\beta \mathbf{m}, \alpha \mathbf{n}} = \sum_{a_0, \dots, a_d} W_{a_0}^{[0]\beta\alpha} W_{a_0 a_1}^{[1]m_0 n_0} \cdots W_{a_{d-1}}^{[d]m_{d-1} n_{d-1}}, \quad (8)$$

where \mathbf{m} and \mathbf{n} include all degrees of freedom, both reactive and non-reactive in this equation. With a second-order Trotter-Suzuki decomposition [45], the

time-evolution operator is given by

$$e^{-i\hat{H}\Delta t} = e^{-i\hat{T}_N\Delta t/2} e^{-i\hat{H}_0\Delta t/2} e^{-i\hat{H}_1\Delta t} e^{-i\hat{H}_0\Delta t/2} e^{-i\hat{T}_N\Delta t/2}. \quad (9)$$

Each component in the propagator can be decomposed into the MPO form. Firstly, the propagator associated with the nuclear kinetic energy operator acting only on the nuclear degrees of freedom becomes

$$\begin{aligned} \mathbf{U}_{T_N} &= \langle \beta \mathbf{m} \boldsymbol{\mu} | e^{-i\hat{T}_N\Delta t} | \alpha \mathbf{n} \boldsymbol{\nu} \rangle \\ &= A_{\mathbf{m}, \mathbf{n}, \alpha} \langle \mathbf{m} | e^{-i\hat{T}_q\Delta t} | \mathbf{n} \rangle \langle \boldsymbol{\mu} | e^{-i\hat{T}_Q\Delta t} | \boldsymbol{\nu} \rangle \end{aligned} \quad (10)$$

Similar to the original ansatz, the reactive coordinate kinetic energy operator is dressed by the electronic overlap matrix $A_{\mathbf{m}, \mathbf{n}, \alpha} = \langle \phi_\beta(\mathbf{q}_m, \mathbf{Q}_0) | \phi_\alpha(\mathbf{q}_n, \mathbf{Q}_0) \rangle_r$. The components $\langle \mathbf{m} | e^{-i\hat{T}_q\Delta t} | \mathbf{n} \rangle$ and $\langle \boldsymbol{\mu} | e^{-i\hat{T}_Q\Delta t} | \boldsymbol{\nu} \rangle$ are separable for each nuclear degree of freedom for rectilinear coordinates, yielding a d -site rank-one MPO $\left(\prod_{k=1}^{d_R} \langle m_k | e^{-i\hat{T}_k\Delta t} | n_k \rangle \right) \left(\prod_{l=1}^{d_{NR}} \langle \mu_l | e^{-i\hat{T}_l\Delta t} | \nu_l \rangle \right)$. The full MPO for \mathbf{U}_{T_N} is then constructed by element-wise product of the MPO for the overlap matrix \mathbf{A} with this rank-one MPO. The bond dimension of the final propagator MPO is $D_k = 1$ for $k = d_R, \dots, d$ and is determined by the MPO representation of \mathbf{A} for the first d_R bonds. A schematic representation of the MPO construction is provided in the Supporting Information (Fig. S1).

Next, regarding the propagator for \hat{H}_0 , the matrix representation of $\hat{H}_0(\mathbf{q})$ is diagonal in the coarse-grained ansatz by construction, as is the matrix representation of the corresponding propagator, \mathbf{U}_{H_0} , with elements $\langle \mathbf{m} \boldsymbol{\beta} | e^{-i\hat{H}_0\Delta t} | \mathbf{n} \boldsymbol{\alpha} \rangle = e^{-iV_{n\alpha}\Delta t} \delta_{mn} \delta_{\beta\alpha}$, where the electronic energies $V_{n\alpha}$ are obtained from quantum chemistry calculations. The resulting high-dimensional diagonal tensor, with elements $e^{-iV_{n\alpha}\Delta t}$, acts as the identity on the nonreactive coordinates and is compressed into an MPO representation using TT-SVD.

Finally, the propagator $\hat{U}_{H_1} = e^{-i\hat{H}_1\Delta t}$ is constructed by splitting it into a product of exponentials for the individual terms.

$$e^{-i\hat{H}_1\Delta t} = \prod_k e^{-i\hat{F}_k\Delta\hat{Q}_k\Delta t} \prod_{k,l} e^{-i\hat{G}_{kl}\Delta\hat{Q}_k\Delta\hat{Q}_l\Delta t/2}. \quad (11)$$

The MPO form for the full propagator is constructed by multiplying the MPOs of each term in the product above, applying a TT-rounding step (Algorithm S3) after each contraction to control the bond dimension. Each operator term in the exponent, $\hat{F}_k(\mathbf{q})\Delta\hat{Q}_k$, is a tensor product of an operator acting on the reactive space and one acting on a single nonreactive nuclear coordinate. Its matrix elements in the nuclear basis are $\langle \beta \mathbf{m} \boldsymbol{\mu} | \hat{F}_k \Delta \hat{Q}_k | \alpha \mathbf{n} \boldsymbol{\nu} \rangle = F_{k,n}^{\beta\alpha} \Delta Q_{k\mu} \delta_{mn} \delta_{\mu\nu}$, with $F_{k,n}^{\beta\alpha} = \int \phi_\beta^*(\mathbf{r}; \mathbf{q}_n, \mathbf{Q}_0) \hat{F}_k(\mathbf{r}; \mathbf{q}_n) \phi_\alpha(\mathbf{r}; \mathbf{q}_n, \mathbf{Q}_0) d\mathbf{r}$. Here, $\Delta Q_{k,\mu} \equiv Q_{k,\mu} - Q_{k,0}$ is the scalar displacement of the k -th degree of freedom. Similarly, the matrix elements for the Hessian operator \hat{G} are $\langle \beta \mathbf{m} \boldsymbol{\mu} | \hat{G}_{kl} \Delta \hat{Q}_k \Delta \hat{Q}_l | \alpha \mathbf{n} \boldsymbol{\nu} \rangle = G_{kl,n}^{\beta\alpha} \Delta Q_{k,\mu} \Delta Q_{l,\mu} \delta_{mn} \delta_{\mu\nu}$, with $G_{kl,n}^{\beta\alpha} =$

$\int \phi_\beta^*(\mathbf{r}; \mathbf{q}_n, \mathbf{Q}_0) \hat{G}_{kl}(\mathbf{r}; \mathbf{q}_n) \phi_\alpha(\mathbf{r}; \mathbf{q}_n, \mathbf{Q}_0) d\mathbf{r}$. Note that only matrix elements between the same molecular configurations are required. A schematic representation of the MPO construction is provided in the Supporting Information (Fig. S2). To obtain the MPO for each individual propagator (e.g., $e^{-i\Delta t \hat{F}_k \Delta \hat{Q}_k}$), we first construct the MPO for the operator in the exponent (e.g., $-i\Delta t \hat{F}_k \Delta \hat{Q}_k$), followed by exponentiation using the scaling and squaring method combined with a Taylor expansion [46].

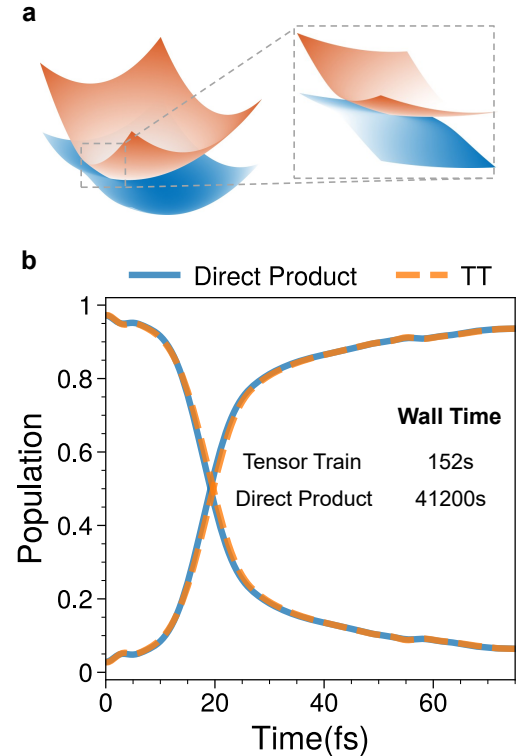


FIG. 1: (a) The adiabatic potential energy surfaces of the S_1 and S_2 states of pyrazine. (b) Time evolution of the electronic population of two states. The result from the coarse-grained method ($\epsilon = 10^{-6}$, $D_{\max} = 100$, orange dashed line) is compared with the benchmark result from the direct product method (blue solid line) over the first 75 fs.

We first demonstrate the accuracy and efficiency of this coarse-grained quantum geometrical molecular dynamics method in tensor-train representation, by simulating the internal conversion dynamics through a conical intersection in the pyrazine molecule following photoexcitation to the S_2 state. It is straightforward to integrate any quantum chemistry method into our approach because a primary advantage of the quantum geometric framework is that the *adiabatic* electronic eigenstates with random gauge choices from electronic structure calculations can be directly employed without gauge fixing or adiabatic-to-diabatic transformation.

Since current electronic structure software does not

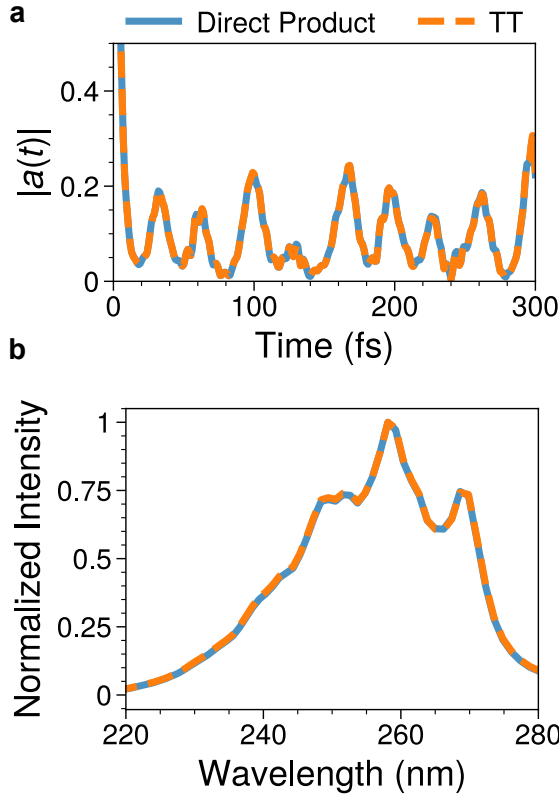


FIG. 2: (a) The absolute value of the autocorrelation function, $|a(t)|$, obtained using the tensor train method compared with the benchmark result from the direct product method. (b) Comparison of the S_2 state absorption spectra calculated by the coarse-grained method and the direct product method.

provide the required matrix elements of the derivative operators $\hat{\mathbf{F}}$ and $\hat{\mathbf{G}}$, we use a reduced two-state four-mode pyrazine model to create the adiabatic input (the adiabatic energies and the electronic overlap matrix). This model includes the most relevant three A_g modes ($\nu_{6a}, \nu_1, \nu_{9a}$) and one B_{1g} mode (ν_{10a}) [47]. For this reduced-scale simulation, a sine DVR basis[48–50] set with $N_k = 15$ basis functions per mode and a time step of $\Delta t = 0.5$ fs were employed. In the coarse-grained ansatz, ν_{10a} and ν_{6a} were selected as the reactive modes. The rounding parameters for the MPS and MPO were set to an absolute error threshold of $\epsilon = 10^{-6}$ and a maximum bond dimension of $D_{\max} = 100$.

The simulation was run for 150 fs, starting from a Gaussian nuclear wavepacket vertically excited to the S_2 state and centered at $\mathbf{R} = \mathbf{0}$, $\Psi_0 = \prod_{i=1}^d (\pi^{-1/4} e^{-1/2 R_i^2}) |S_2\rangle$, which is represented as a matrix product state. The reference geometry for the non-reactive modes was the Franck-Condon point ($\mathbf{Q}_0 = \mathbf{0}$). The coarse-grained method is in excellent agreement with the fine-grained direct product method for both the electronic population dynamics (Fig. 1) and

the optical absorption spectrum (Fig. 2). This accuracy is achieved with a significant computational speed up: the simulation with tensor network is two orders of magnitude faster than the direct product method (152 s of wall time vs. 41 200 s). In Fig. 2(a), the absolute value of the autocorrelation function is given by $a(t) = \langle \Psi_0 | \Psi(t) \rangle = \langle \Psi(t/2)^* | \Psi(t/2) \rangle$. The corresponding absorption spectrum presented in Fig. 2(b) is calculated as the Fourier transform of the autocorrelation function: $I(\omega) = \int_{-\infty}^{\infty} dt a(t) e^{i\omega t} e^{-|t|/\tau_h} \cos(\frac{\pi t}{2T})$, where $\tau_h = 30$ fs is a damping time and T is the total simulation time.

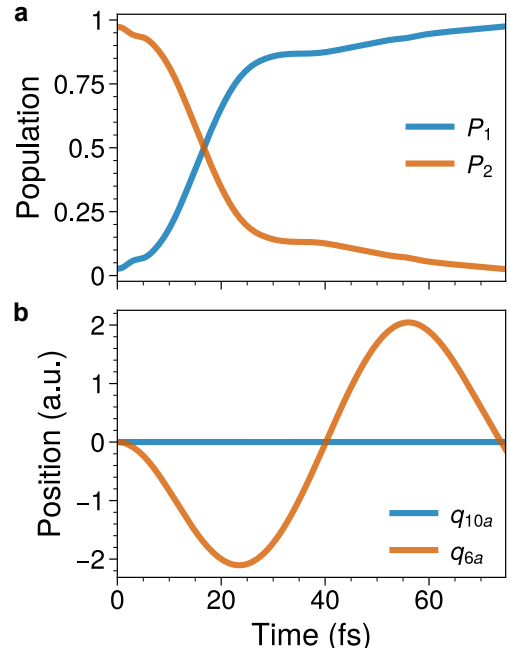


FIG. 3: Nonadiabatic conical intersection dynamics for the full 24-mode pyrazine model. (a) Electronic populations of the initially state S_2 , and the lower-lying state S_1 . (b) Expectation values of the position for the coupling mode q_{10a} , and the tuning mode q_{6a} .

To demonstrate the capability of our method for high-dimensional conical intersection dynamics, we now apply it to the internal conversion dynamics in the full-dimensional pyrazine system with $d = 24$, far beyond the capability of direct-product method. The ν_{6a} and ν_{10a} modes are chosen as reactive modes and the rest as nonreactive modes. A sine DVR basis was used for all modes with $N_k = 15$ basis functions per mode. The time step was set to $\Delta t = 0.5$ fs, the TT-rounding error threshold to $\epsilon = 10^{-6}$, and the maximum bond dimension to $D_{\max} = 40$. The reference geometry for the nonreactive modes was chosen as $\mathbf{Q}_0 = \mathbf{0}$ corresponding to the ground state minimum. The model Hamiltonian is only used to generate the adiabatic input including electronic energies along the reactive coordinates and the nuclear gradients \mathbf{F} and \mathbf{G} ; its analytic form is not

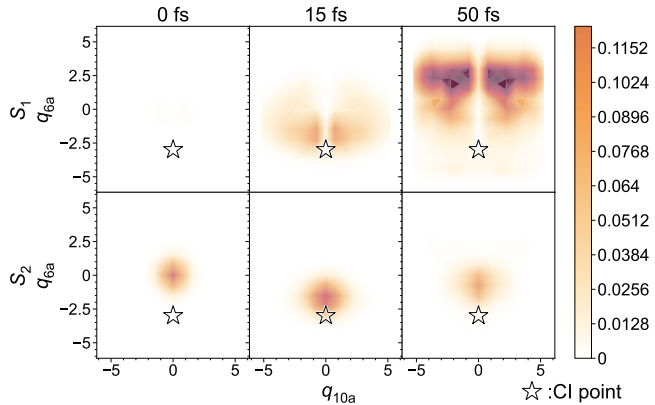


FIG. 4: Reduced probability densities for the 24-mode pyrazine model on the S_2 (bottom) and S_1 (top) surfaces. The densities are projected onto the branching plane spanned by the coupling mode q_{10a} and the tuning mode q_{6a} . The position of the conical intersection is indicated by a star. The wavepacket is initially excited to the S_2 state. At 50 fs, the density transferred to the S_1 surface exhibits a nodal line along $q_{10a} = 0$, a signature of the geometric phase effect induced by the conical intersection.

explicitly used in constructing the MPO. We also start with a Gaussian wavepacket centered at $\mathbf{R} = \mathbf{0}$ vertically excited to the S_2 state $|\Psi_0\rangle = (\prod_{i=1}^d \pi^{-1/4} e^{-\frac{1}{2} R_i^2}) |S_2\rangle$. As shown in Fig. 3 (a), the coarse-grained method successfully captured the ultrafast electronic relaxation dynamics from S_2 to S_1 within ~ 30 fs timescale. The dynamics of the two reactive coordinates are shown in Fig. 3 (b). The expectation value of $\langle q_{6a}(t) \rangle$ (orange line), exhibits significant oscillatory motion, indicating that the nuclear wavepacket moves along this coordinate upon passing through the conical intersection. The wavepacket reaches its first maximum displacement at approximately 25 fs and oscillates. In contrast, the expectation value of the coupling mode position, $\langle q_{10a}(t) \rangle$ (blue line), remains at 0 throughout the entire simula-

tion due to the mirror symmetry of the model with respect to this coordinate, as expected. There is, nevertheless, significant diffusion along this mode occurring during the dynamics, see Fig. 4. For the reduced probability densities projected onto the two reactive coordinates q_{6a} and q_{10a} , $\rho_k(\mathbf{q}, t) = \int |\Psi_k(\mathbf{q}, \mathbf{Q}, t)|^2 d\mathbf{Q}$. At $t = 0$ fs, the wavepacket is centrally localized on the S_2 surface. As the population transfers to the S_1 surface, the wavepacket undergoes significant spreading. Crucially, at $t = 50$ fs, the density formed on the S_1 surface exhibits a distinct double-lobe structure with a nodal plane along $q_{10a} = 0$, where the probability density vanishes. This nodal feature is a manifestation of the geometric phase effects. Our method remains stable at longer times beyond the first passage through the conical intersection, see Fig. S7 for a longer time simulation up to 150 fs, with 14 hours of wall time.

To summarize, we have introduced a coarse-grained geometric quantum dynamics framework in the tensor-network representation for high-dimensional strongly coupled electron-nuclear dynamics. It allows direct *ab initio* simulation of conical intersection dynamics incorporating all non-Born–Oppenheimer effects including not only nonadiabatic coupling but also geometric phase effect, diagonal Born–Oppenheimer correction, and second-order derivative couplings. It does not require a pre-constructed global diabatic analytic Hamiltonian or approximate quasi-diabatization to remove singular derivative couplings. The accuracy and efficiency of the method are demonstrated first by a four-dimensional pyrazine model followed by a full-dimensional nonadiabatic quantum molecular dynamics modeling. The results imply that the geometric quantum dynamics provides a powerful tool for direct modeling of high-dimensional quantum dynamics at conical intersections from first principles without constructing a diabatic model Hamiltonian. The coarse-graining scheme employed here is a simple version when reactive coordinates can be clearly identified; for more complex reactions, an automatic algorithm can be developed for the coarse-graining step.

[1] C. A. Mead, The geometric phase in molecular systems, *Reviews of Modern Physics* **64**, 51 (1992).

[2] W. Domcke, D. R. Yarkony, and H. Köppel, *Conical Intersections: Theory, Computation and Experiment* (World Scientific, 2011).

[3] F. J. Garcia-Vidal, C. Ciuti, and T. W. Ebbesen, Manipulating Matter by Strong Coupling to Vacuum Fields, *Science* **373**, eabd0336 (2021).

[4] J. Larson, E. Sjöqvist, and P. Öhberg, *Conical Intersections in Physics: An Introduction to Synthetic Gauge Theories*, Lecture Notes in Physics, Vol. 965 (Springer International Publishing, Cham, 2020).

[5] D. Polak, R. Jayaprakash, T. P. Lyons, L. Á. Martínez-Martínez, A. Leventis, K. J. Fallon, H. Coulthard, D. G. Bossanyi, K. Georgiou, I. I. Anthony J. Petty, J. Anthony, H. Bronstein, J. Yuen-Zhou, A. I. Tartakovskii, J. Clark, and A. J. Musser, Manipulating molecules with strong coupling: Harvesting triplet excitons in organic exciton microcavities, *Chemical Science* **11**, 343 (2020).

[6] D. Polli, P. Altoè, O. Weingart, K. M. Spillane, C. Manzoni, D. Brida, G. Tomasello, G. Orlandi, P. Kukura, R. A. Mathies, M. Garavelli, and G. Cerullo, Conical intersection dynamics of the primary photoisomerization event in vision, *Nature* **467**, 440 (2010).

[7] S. Rafiq, N. P. Weingartz, S. Kromer, F. N. Castellano, and L. X. Chen, Spin–vibronic coherence drives singlet–triplet conversion, *Nature* **620**, 776 (2023).

[8] H. J. Wörner, J. B. Bertrand, B. Fabre, J. Higuet, H. Ruf,

A. Dubrouil, S. Patchkovskii, M. Spanner, Y. Mairesse, V. Blanchet, E. Mével, E. Constant, P. B. Corkum, and D. M. Villeneuve, Conical Intersection Dynamics in NO₂ Probed by Homodyne High-Harmonic Spectroscopy, *Science* **334**, 208 (2011).

[9] I. G. Ryabinkin, L. Joubert-Doriol, and A. F. Izmaylov, Geometric Phase Effects in Nonadiabatic Dynamics near Conical Intersections, *Accounts of Chemical Research* **50**, 1785 (2017).

[10] J. Wang, C. Xie, X. Hu, H. Guo, and D. Xie, Impact of Geometric Phase on Dynamics of Complex-Forming Reactions: H + O₂ → OH + O, *The Journal of Physical Chemistry Letters* **15**, 4237 (2024).

[11] C. Xie, B. K. Kendrick, D. R. Yarkony, and H. Guo, Constructive and Destructive Interference in Nonadiabatic Tunneling via Conical Intersections, *Journal of Chemical Theory and Computation* **13**, 1902 (2017).

[12] B. Kendrick, Geometric Phase Effects in the Vibrational Spectrum of Na 3 (X), *Physical Review Letters* **79**, 2431 (1997).

[13] C. Xie, J. Ma, X. Zhu, D. R. Yarkony, D. Xie, and H. Guo, Nonadiabatic Tunneling in Photodissociation of Phenol, *Journal of the American Chemical Society* **138**, 7828 (2016).

[14] D. Yuan, Y. Guan, W. Chen, H. Zhao, S. Yu, C. Luo, Y. Tan, T. Xie, X. Wang, Z. Sun, D. H. Zhang, and X. Yang, Observation of the geometric phase effect in the H + HD → H₂ + D reaction, *Science* **362**, 1289 (2018).

[15] C. A. Mead and D. G. Truhlar, Conditions for the definition of a strictly diabatic electronic basis for molecular systems, *Journal of Chemical Physics* **77**, 6090 (1982).

[16] W. Zhou, A. Mandal, and P. Huo, Quasi-Diabatic Scheme for Nonadiabatic On-the-Fly Simulations, *Journal of Physical Chemistry Letters* **10**, 7062 (2019).

[17] D. R. Yarkony, C. Xie, X. Zhu, Y. Wang, C. L. Malbon, and H. Guo, Diabatic and adiabatic representations: Electronic structure caveats, *Computational and Theoretical Chemistry* **1152**, 41 (2019).

[18] D. A. Fedorov and B. G. Levine, A discontinuous basis enables numerically exact solution of the Schrödinger equation around conical intersections in the adiabatic representation, *Journal of Chemical Physics* **150**, 054102 (2019).

[19] J. E. Subotnik, S. Yeganeh, R. J. Cave, and M. A. Ratner, Constructing diabatic states from adiabatic states: Extending generalized Mulliken–Hush to multiple charge centers with Boys localization, *Journal of Chemical Physics* **129**, 244101 (2008).

[20] S. Choi and J. Vaníček, Which form of the molecular hamiltonian is the most suitable for simulating the nonadiabatic quantum dynamics at a conical intersection?, *Journal of Chemical Physics* **153**, 211101 (2020).

[21] D. J. Tannor, *Introduction to Quantum Mechanics: A Time-Dependent Perspective* (University Science Books, 2007).

[22] X. Zhu and D. R. Yarkony, On the Construction of Property Based Diabatizations: Diabolical Singular Points, *Journal of Physical Chemistry A* **119**, 12383 (2015).

[23] G. A. Worth, H.-D. Meyer, and L. S. Cederbaum, Multidimensional dynamics involving a conical intersection: Wavepacket calculations using the mctdh method, in *Advanced Series in Physical Chemistry*, Vol. 15 (WORLD SCIENTIFIC, 2004) pp. 583–617.

[24] H. Wang and M. Thoss, Multilayer formulation of the multiconfiguration time-dependent hartree theory, *Journal of Chemical Physics* **119**, 1289 (2003).

[25] M. A. Cazalilla, Time-dependent density-matrix renormalization group: A systematic method for the study of quantum many-body out-of-equilibrium systems, *Physical Review Letters* **88**, 10.1103/PhysRevLett.88.256403 (2002).

[26] U. Schollwöck, The density-matrix renormalization group: A short introduction, *Philosophical Transactions of the Royal Society A: Mathematical, Physical and Engineering Sciences* **369**, 2643 (2011).

[27] U. Schollwöck, The density-matrix renormalization group in the age of matrix product states, *Annals of Physics* **326**, 96 (2011).

[28] F. Aleotti, D. Aranda, M. Yaghoubi Jouybari, M. Garavelli, A. Nenov, and F. Santoro, Parameterization of a Linear Vibronic Coupling Model with Multiconfigurational Electronic Structure Methods to Study the Quantum Dynamics of Photoexcited Pyrene, *J. Chem. Phys.* **154**, 104106 (2021).

[29] A. Mandal, S. S. Yamijala, and P. Huo, Quasi-Diabatic Representation for Nonadiabatic Dynamics Propagation, *Journal of Chemical Theory and Computation* **14**, 1828 (2018).

[30] Y. Guan, C. Xie, D. R. Yarkony, and H. Guo, High-fidelity first principles nonadiabaticity: Diabatization, analytic representation of global diabatic potential energy matrices, and quantum dynamics, *Physical Chemistry Chemical Physics* **23**, 24962 (2021).

[31] Y. Xie, R. Liu, and B. Gu, Quantum geometrical molecular dynamics, *Science Advances* **11**, eadz3711 (2025).

[32] B. Gu, A Discrete-Variable Local Diabatic Representation of Conical Intersection Dynamics, *Journal of Chemical Theory and Computation* **19**, 6557 (2023).

[33] B. Gu, Nonadiabatic Conical Intersection Dynamics in the Local Diabatic Representation with Strang Splitting and Fourier Basis, *Journal of Chemical Theory and Computation* **20**, 2711 (2024).

[34] M. Sha and B. Gu, Exponential convergence of the local diabatic representation for nonadiabatic models (2025), arXiv:2509.05694 [physics].

[35] X. Zhu and B. Gu, Making Peace with Random Phases: Ab Initio Conical Intersection Quantum Dynamics in Random Gauges, *The Journal of Physical Chemistry Letters* **15**, 8487 (2024).

[36] C. A. Mead and D. G. Truhlar, On the determination of Born–Oppenheimer nuclear motion wave functions including complications due to conical intersections and identical nuclei, *Journal of Chemical Physics* **70**, 2284 (1979).

[37] Y. Xie and B. Gu, Linked product approximation to the global electronic overlap matrix, *Journal of Chemical Theory and Computation* **21**, 9249 (2025).

[38] Y. Xie, Y. Yang, X. Zhu, A. Chen, and B. Gu, Nondirect-Product Local Diabatic Representation with Smolyak Sparse Grids, *Journal of Chemical Theory and Computation* **20**, 9512 (2024).

[39] T. Frankel, *The Geometry of Physics: An Introduction*, 3rd ed. (Cambridge University Press, Cambridge, 2011).

[40] I. V. Oseledets, Tensor-Train Decomposition, *SIAM Journal on Scientific Computing* **33**, 2295 (2011).

[41] Y. Zhang and E. Solomonik, On stability of tensor networks and canonical forms (2020), arXiv:2001.01191 [math].

[42] G. K.-L. Chan and M. Head-Gordon, Highly correlated calculations with a polynomial cost algorithm: A study of the density matrix renormalization group, *Journal of Chemical Physics* **116**, 4462 (2002).

[43] K. Kinjo, R. Sakurai, T. Kishimoto, and J. Ohkubo, Permutation of Tensor-Train Cores for Computing Moments on Stochastic Differential Equations, *Journal of the Physical Society of Japan* **94**, 084001 (2025), arXiv:2504.10492 [physics].

[44] V. Murg, V. E. Korepin, and F. Verstraete, Algebraic Bethe ansatz and tensor networks, *Physical Review B* **86**, 045125 (2012).

[45] M. Suzuki, Generalized trotter's formula and systematic approximants of exponential operators and inner derivations with applications to many-body problems, *Communications in Mathematical Physics* **51**, 183 (1976).

[46] N. J. Higham, The Scaling and Squaring Method for the Matrix Exponential Revisited, *SIAM Journal on Matrix Analysis and Applications* **26**, 1179 (2005).

[47] A. Raab, G. A. Worth, H.-D. Meyer, and L. S. Cederbaum, Molecular dynamics of pyrazine after excitation to the S2 electronic state using a realistic 24-mode model Hamiltonian, *Journal of Chemical Physics* **110**, 936 (1999).

[48] D. T. Colbert and W. H. Miller, A novel discrete variable representation for quantum mechanical reactive scattering via the S -matrix Kohn method, *Journal of Chemical Physics* **96**, 1982 (1992).

[49] J. C. Light, I. P. Hamilton, and J. V. Lill, Generalized discrete variable approximation in quantum mechanics, *Journal of Chemical Physics* **82**, 1400 (1985).

[50] J. C. Light and T. Carrington, Discrete-Variable Representations and their Utilization, in *Advances in Chemical Physics*, Vol. 114, edited by I. Prigogine and S. A. Rice (Wiley, 2000) 1st ed., pp. 263–310.

Supplementary Information for
“Coarse-Grained Geometric Quantum Dynamics in the Tensor
Network Representation”

I. TENSOR TRAIN ALGORITHM USED IN THIS WORK

Algorithm S1 Tensor-Train SVD (TT-SVD)

Input: A d -dimensional tensor \mathbf{A} of size $n_0 \times \cdots \times n_{d-1}$.

Parameters: Decomposition error ϵ , max bond dimension D_{\max} .

Output: TT-cores $\mathbf{A}^{[0]}, \dots, \mathbf{A}^{[d-1]}$.

```

1:  $\mathbf{C}_{\text{res}} \leftarrow \mathbf{A}$                                  $\triangleright$  Initialize residual tensor
2:  $D_{\text{left}} \leftarrow 1$ 
3: for  $k = 0$  to  $d - 2$  do
4:    $\mathbf{M} \leftarrow \text{reshape}(\mathbf{C}_{\text{res}}, [D_{\text{left}} \cdot n_k, -1])$ 
5:    $(\mathbf{U}, \mathbf{\Sigma}, \mathbf{V}) \leftarrow \text{TruncatedSVD}(\mathbf{M}, \delta = \epsilon/\sqrt{d-1}, D_{\max})$        $\triangleright$  Detailed in Algorithm S2
6:    $D_{\text{right}} \leftarrow \text{size}(\mathbf{\Sigma}, 1)$ 
7:    $\mathbf{A}^{[k]} \leftarrow \text{reshape}(\mathbf{U}, [D_{\text{left}}, n_k, D_{\text{right}}])$ 
8:    $\mathbf{C}_{\text{res}} \leftarrow \mathbf{\Sigma} \mathbf{V}^T$ 
9:    $D_{\text{left}} \leftarrow D_{\text{right}}$ 
10: end for
11:  $\mathbf{A}^{[d-1]} \leftarrow \mathbf{C}_{\text{res}}$ 

```

Algorithm S2 Truncated SVD Procedure

Input: Matrix \mathbf{M} .

Parameters: Local truncation error δ , max rank D_{\max} .

Output: Truncated error $\mathbf{U}', \mathbf{\Sigma}', \mathbf{V}'$.

```

1: Perform SVD:  $\mathbf{M} = \mathbf{U} \mathbf{\Sigma} \mathbf{V}^T$  with singular values  $\sigma_0 \geq \sigma_1 \geq \cdots \geq 0$ .
2: Find the smallest integer  $D$  such that  $\sqrt{\sum_{j=D}^{\text{end}} \sigma_j^2} \leq \delta$ .
3: if  $D_{\max}$  is provided then
4:    $D \leftarrow \min(D, D_{\max})$ 
5: end if
6:  $\mathbf{U}' \leftarrow \mathbf{U}(:, 0 : D)$ 
7:  $\mathbf{\Sigma}' \leftarrow \mathbf{\Sigma}(0 : D, 0 : D)$ 
8:  $\mathbf{V}' \leftarrow \mathbf{V}(:, 0 : D)$ 
9: return  $\mathbf{U}', \mathbf{\Sigma}', \mathbf{V}'$ 

```

Algorithm S3 TT-rounding

Input: A d -dimensional left-canonical tensor train \mathbf{A} .

Parameters: Truncation error ϵ , max bond dimension D_{\max} .

Output: Compressed tensor train \mathbf{A}' .

```

1:  $\mathbf{A}' \leftarrow \mathbf{A}$ 
2: for  $k = d - 1$  down to 1 do
3:    $D_k, n_k, D_{k+1} \leftarrow \text{size}(\mathbf{A}'^{[k]})$ 
4:    $\mathbf{M} \leftarrow \text{reshape}(\mathbf{A}'^{[k]}, [D_k, n_k \cdot D_{k+1}])$ 
5:    $(\mathbf{U}, \mathbf{\Sigma}, \mathbf{V}) \leftarrow \text{TruncatedSVD}(\mathbf{M}, \delta = \epsilon/\sqrt{d-1}, D_{\max})$             $\triangleright$  Detailed in Algorithm S2
6:    $D'_k \leftarrow \text{size}(\mathbf{\Sigma}, 1)$ 
7:    $\mathbf{A}'^{[k]} \leftarrow \text{reshape}(\mathbf{V}^T, [D'_k, n_k, D_{k+1}])$ 
8:    $\mathbf{A}'^{[k-1]} \leftarrow \text{reshape}(\mathbf{A}'^{[k-1]}, [-1, D_k]) \cdot (\mathbf{U}\mathbf{\Sigma})$             $\triangleright$  Absorb U into previous core
9:    $\mathbf{A}'^{[k-1]} \leftarrow \text{reshape}(\mathbf{A}'^{[k-1]}, [D_{k-1}, n_{k-1}, D'_k])$ 
10: end for
11: return  $\mathbf{A}'$ 

```

The accuracy of TT-SVD and TT-rounding is governed by the singular value truncation at each step. The local truncation error is quantified by the square root of the sum of the squares of the discarded singular values [1–3]:

$$\delta = \sqrt{\sum_{j=D} \sigma_j^2}, \quad (\text{S1})$$

where σ_j are the singular values arranged in descending order. A uniform local error threshold δ yields a total error of $\epsilon = \delta\sqrt{d-1}$. However, slowly decaying singular values—typical in strongly entangled systems—can lead to excessive bond dimensions. To ensure computational feasibility, we employ a hybrid truncation strategy as detailed in Algorithm S2. The retained rank D is first determined by the error threshold δ and subsequently capped by a hard limit D_{\max} , such that the final rank is given by $\min(D, D_{\max})$.

II. CONSTRUCTION OF THE PROPAGATORS IN THE TENSOR TRAIN REPRESENTATION

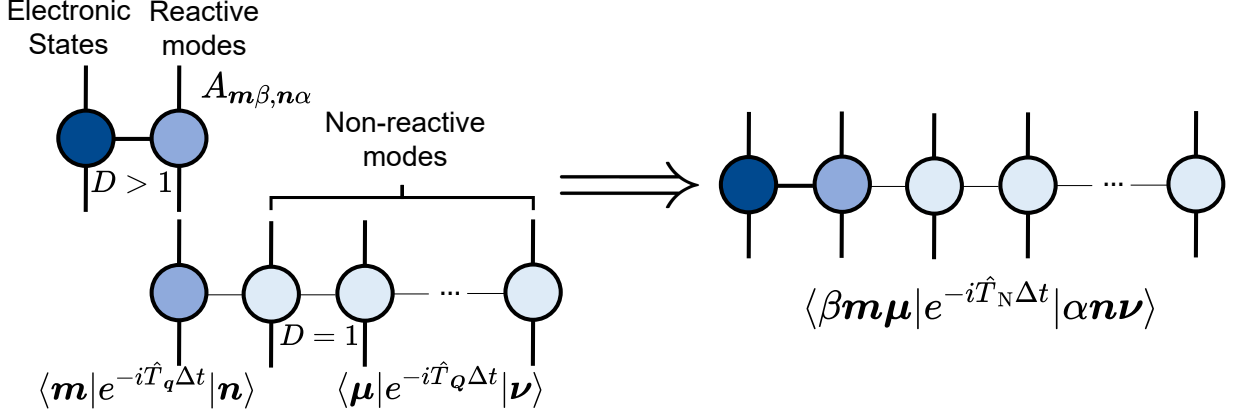


FIG. S1: Schematic construction of the kinetic energy propagator $e^{-i\hat{T}_N\Delta t}$ in the coarse-grained method. The line width schematically represents the corresponding bond dimension. Different colors represent different types of indices.

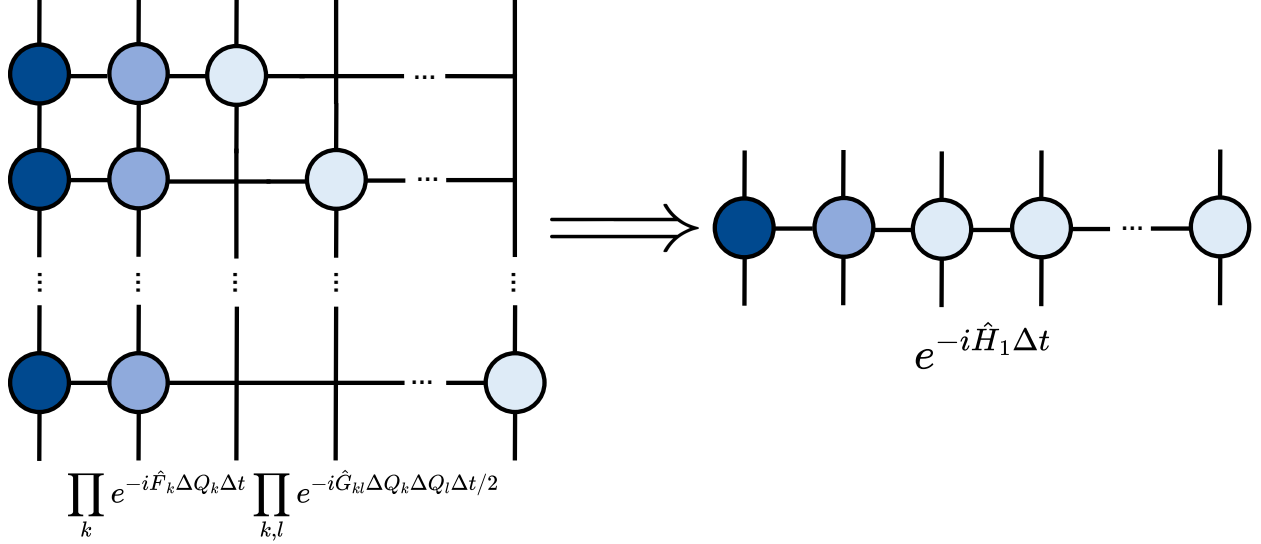


FIG. S2: Schematic construction of the propagator $e^{-i\hat{H}_1\Delta t}$ in the coarse-grained method. For clarity, only $\prod_k e^{-i\hat{F}_k \Delta Q_k \Delta t}$ is shown. The line width schematically represents the corresponding bond dimension. The empty intersections correspond to identity matrices at the corresponding sites. Different colors represent different types of indices.

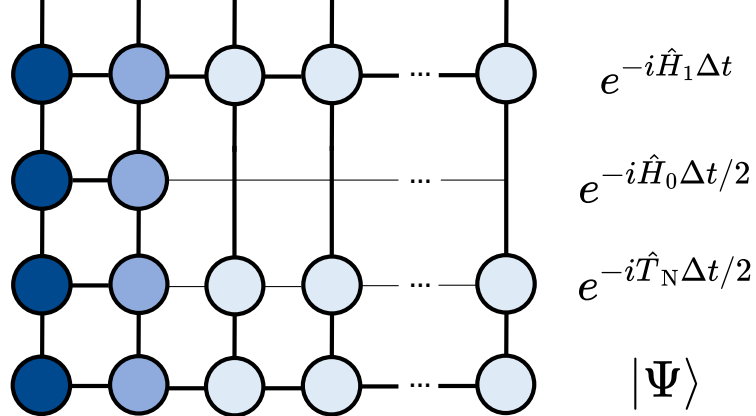


FIG. S3: Schematic construction of a half-step evolution of the wavefunction in the coarse-grained method. The line width schematically represents the corresponding bond dimension. $|\psi\rangle$ represents the wavefunction at the current time step. Different colors represent different types of indices.

III. VIBRONIC COUPLING MODEL FOR PYRAZINE

The vibronic coupling Hamiltonian is given by

$$\hat{H} = \sum_i \frac{\omega_i}{2} \left(-\frac{\partial^2}{\partial R_i^2} + \hat{R}_i^2 \right) \mathbf{I} + \begin{bmatrix} -\Delta & 0 \\ 0 & \Delta \end{bmatrix} + \sum_{i \in G_1} \begin{bmatrix} a_i & 0 \\ 0 & b_i \end{bmatrix} \hat{R}_i + \sum_{i \in G_3} \begin{bmatrix} 0 & c_i \\ c_i & 0 \end{bmatrix} \hat{R}_i \\ + \sum_{(i,j) \in G_2} \begin{bmatrix} a_{i,j} & 0 \\ 0 & b_{i,j} \end{bmatrix} \hat{R}_i \hat{R}_j + \sum_{(i,j) \in G_4} \begin{bmatrix} 0 & c_{i,j} \\ c_{i,j} & 0 \end{bmatrix} \hat{R}_i \hat{R}_j \quad (S2)$$

where \mathbf{I} is the identity matrix, ω_i denotes the ground-state vibrational frequency of the i -th normal mode, R_i is the corresponding dimensionless normal-mode coordinate. G_i refers to four different symmetry groups of the vibrational modes. The parameters are extracted from reference[4].

IV. ERROR ANALYSIS

The error in the coarse-grained method arises from three main sources: the Trotter error from the time-stepping algorithm ($\mathcal{O}(\Delta t^3)$), the truncation error in TT-SVD and TT-rounding, and the error originating from the coarse-grained ansatz. The Trotter error can be systematically controlled by reducing the time step Δt . In this section, we focus on analyzing the truncation error and the coarse-graining error.

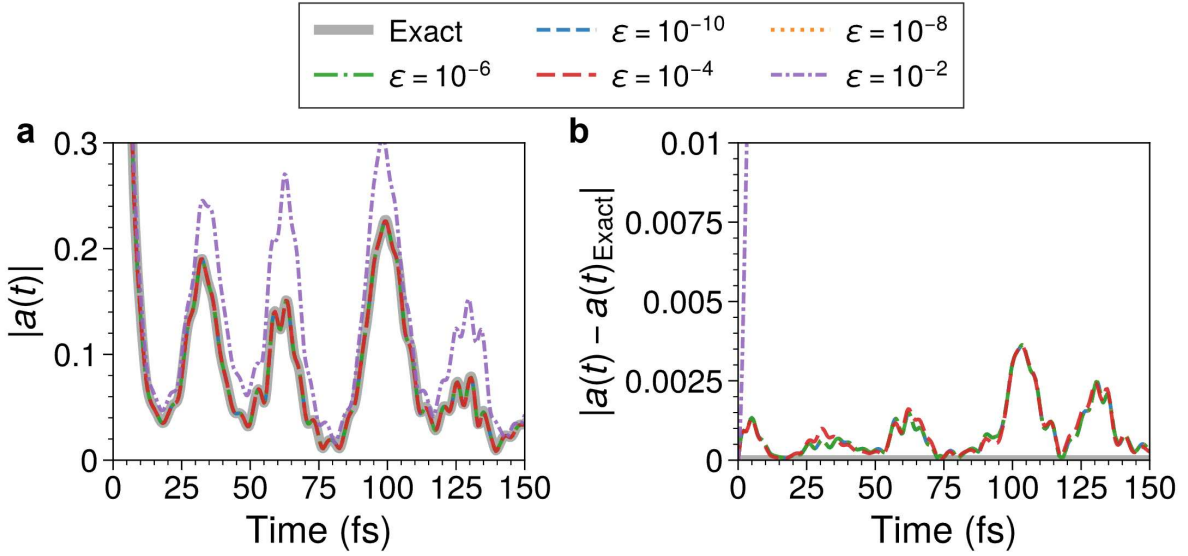


FIG. S4: Error analysis of the calculation with respect to the truncation error ϵ . (a) The absolute value of the autocorrelation function, $|a(t)|$, calculated with different ϵ values, compared to the exact result. (b) The absolute difference in $|a(t)|$ between the TT calculations and the exact result.

First, we investigate the effect of the truncation error parameter ϵ . We set the maximum bond dimension $D_{\max} = 200$, ensuring that the truncation error is predominantly governed by ϵ . Fig. S4 demonstrates that the autocorrelation function, defined as $a(t) = \langle \Psi(0) | \Psi(t) \rangle$, converges rapidly with respect to this parameter. A threshold of $\epsilon = 10^{-6}$ is sufficient to achieve excellent agreement. The simulation with this parameter required approximately 137 seconds of wall time. The maximum RAM required, assuming the “complex128” data type, was approximately 40 GB, while the compressed file containing states and operators occupied less than 200 MB. The bond dimension reached a maximum of 98 at the virtual bond connecting the reactive and non-reactive coordinates.

Next, we test the convergence with respect to D_{\max} . To isolate its effect, we set the error threshold ϵ to a value near machine precision (10^{-14}), ensuring that truncation is exclusively determined by D_{\max} . As shown in Fig. S5, increasing D_{\max} systematically improves accuracy, with the autocorrelation function fully converging for D_{\max} in the range of 40 to 50. For the case of $D_{\max} = 40$, the simulation required approximately 8000 seconds of wall time, with a theoretical peak transient memory of approximately 17 GB for the complex128 wavefunction,

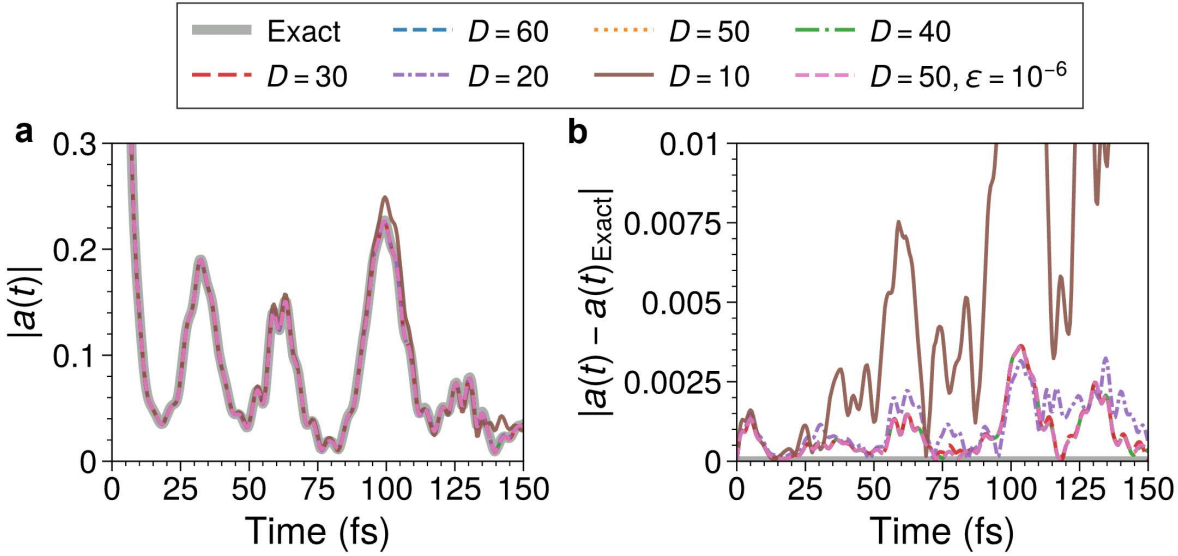


FIG. S5: Error analysis of the calculation with respect to different maximum bond dimension D_{\max} . (a) The absolute value of the autocorrelation function, $|a(t)|$, calculated with different D_{\max} values, compared to the exact result. (b) The absolute difference in $|a(t)|$ between the TT calculations and the exact result.

while the size of the saved wavepacket file at each time step was approximately 120 MB. However, by introducing a practical error threshold of $\epsilon = 10^{-6}$ with a sufficient $D_{\max} = 50$, a result of comparable accuracy is obtained (see Fig. S5), while the computational cost is dramatically reduced: the approximate wall time decreases to 152 seconds, with a peak transient memory of approximately 3 GB and a file size per time step of approximately 143 MB. Notably, the rapid convergence with respect to D_{\max} suggests that the 4-mode pyrazine model does not generate high levels of entanglement, making it particularly well-suited for the TT approach.

Finally, we assess the influence of the reference geometry for non-reactive coordinates, \mathbf{Q}_0 , a critical parameter in our coarse-graining approach. As the reference point for the Taylor expansion of the Hamiltonian, its choice directly determines the quality of the approximated potential energy surfaces. To investigate this dependence, we performed simulations using four distinct geometries:

- (i) The ground state minimum point $\mathbf{Q}_0 = (0, 0)$.
- (ii) The projection of the minimum energy point of the conical intersection hypersurface

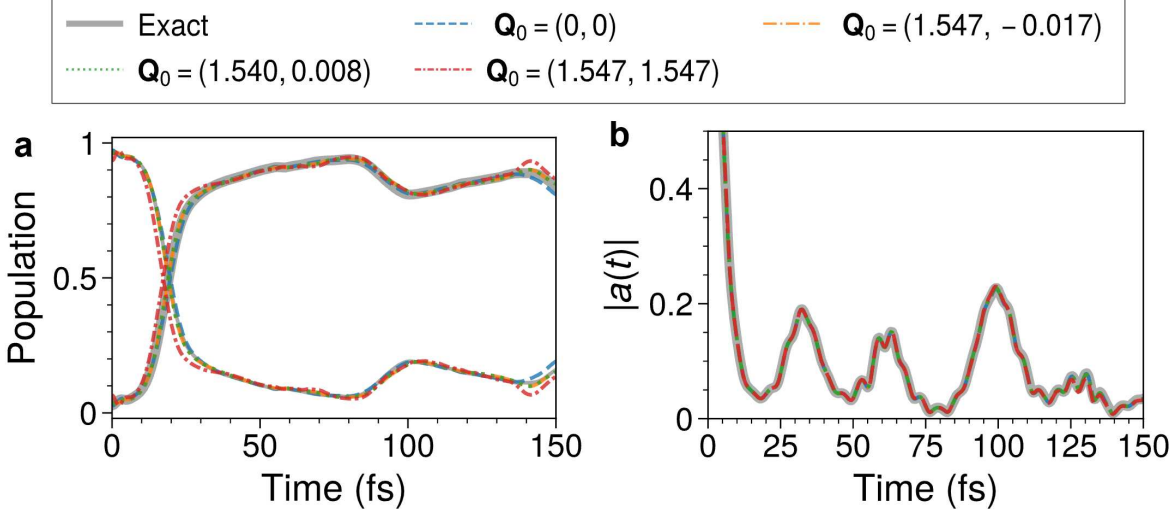


FIG. S6: Influence of the reference geometry \mathbf{Q}_0 on the TT calculation. (a) Time evolution of the electronic population of the S_2 state for four different choices of \mathbf{Q}_0 , compared to the exact result. (b) The absolute difference in the autocorrelation function $|a(t)|$ relative to the exact result for each choice of \mathbf{Q}_0 .

for the 4-mode model, $\mathbf{Q}_0 = (1.547, -0.017)$, for modes (ν_1, ν_{9a}) [4].

- (iii) The projection of the minimum energy point of the conical intersection hypersurface for the 24-mode model, $\mathbf{Q}_0 = (1.540, 0.008)$, for modes (ν_1, ν_{9a}) [4].
- (iv) An arbitrarily chosen geometry $\mathbf{Q}_0 = (1.547, 1.547)$.

The choice of the reference point \mathbf{Q}_0 influences the overall relaxation dynamics, with different physically motivated geometries performing better for different observables. Setting \mathbf{Q}_0 at the Franck-Condon point (i) yields a more accurate autocorrelation function, whereas choosing the conical intersection minima (ii and iii) results in more accurate population dynamics. In contrast, the arbitrary geometry (iv) produces large discrepancies in both autocorrelation and population dynamics. Hence, the predictive accuracy of the method depends sensitively on selecting a physically appropriate reference geometry.

V. LONG-TIME DYNAMICS

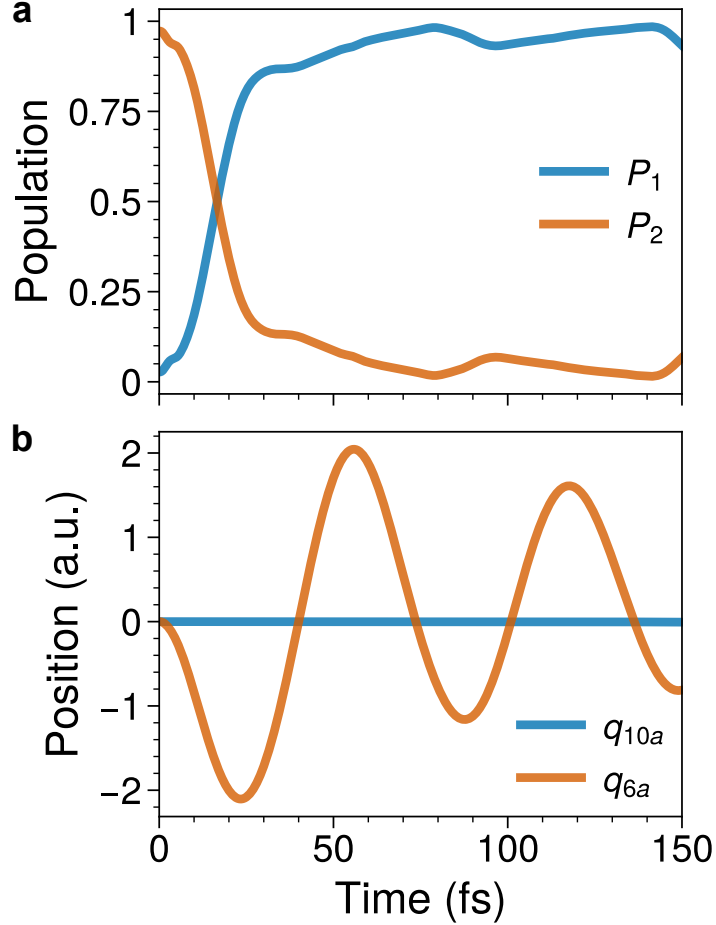


FIG. S7: Non-adiabatic dynamics of the full 24-mode pyrazine model over 150 fs. (a) Electronic population dynamics of the initially excited state S_2 and the lower-lying state S_1 . (b) Position expectation values for the coupling mode q_{10a} and the tuning mode q_{6a} .

[1] C. Eckart and G. Young, The Approximation of One Matrix by Another of Lower Rank, *Psychometrika* **1**, 211 (1936).

[2] L. MIRSKY, SYMMETRIC GAUGE FUNCTIONS AND UNITARILY INVARIANT NORMS, *The Quarterly Journal of Mathematics* **11**, 50 (1960).

[3] I. V. Oseledets, Tensor-Train Decomposition, *SIAM Journal on Scientific Computing* **33**, 2295 (2011).

[4] A. Raab, G. A. Worth, H.-D. Meyer, and L. S. Cederbaum, Molecular dynamics of pyrazine after excitation to the S2 electronic state using a realistic 24-mode model Hamiltonian, *Journal of Chemical Physics* **110**, 936 (1999).